## PAPER

Check for updates

# Three-dimensional graphene-supported nickel disulfide nanoparticles promise stable and fast potassium storage†

Kang Han,[a] Jiashen Meng,[a] Xufeng Hong,[a] Xuanpeng Wang ID *[b] and Liqiang Mai ID *[a]

Nickel sulfide ($NiS_2$) is generally regarded as an appropriate anode for manufacturing new-type potassium-ion batteries (PIBs), while the development and application of $NiS_2$ are hampered by poor intrinsic electrical conductivity and huge volumetric change during potassiation/de-potassiation. Herein, we construct self-adaptive $NiS_2$ nanoparticles confined to a three-dimensional graphene oxide ($NiS_2$/3DGO) electrode *via in situ* sulfurization and self-assembly processes. The as-obtained $NiS_2$/3DGO exhibits high reversible capacity (391 mA h g$^{-1}$) and outstanding rate behavior (stable cycling at 1000 mA g$^{-1}$) for PIBs. Furthermore, *in situ* X-ray diffractometry and *ex situ* Raman test results elucidate partially reversible transformation from the cubic $NiS_2$ phase to the $K_xNiS_2$ intermediate, followed by generating a $Ni^0$ and $K_2S_4$ product. This phenomenon is caused by the conversion reaction mechanism of $NiS_2$ nanocrystals along with an amorphous phase transition during the initial cycle. Such understandings may shed new light on the application of metal sulfides and give directions to design novel electrodes with desirable structural stability and lifespan.

## Introduction

With the popularization of 5th generation (5G) wireless systems and the Internet of Things (IoT) technologies, the era in which everything is interconnected has set in motion a new wave in energy revolution.[1] Nowadays, lithium-ion batteries (LIBs) have been widely used in all aspects of our life and almost entirely equipped with mobile terminal equipment.[1–3] Nevertheless, considering the uneven distribution of lithium resources (0.0017 wt%) and high prices,[4] the economic benefits of LIBs for grid-scale energy storage are less attractive. Researchers have gradually turned their attention to potassium-ion batteries (PIBs) owing to their sustainable competitive advantages of abundant potassium reserves (1.5 wt%), high operating voltage, and fast ion conductivity in electrolytes.[4] Compared with that of sodium, the standard reduction potential of potassium is more near to lithium,[4,5] which brings

about a relatively high energy density of the PIBs. Besides, aluminium foil can be substituted in place of copper foil as a current collector at the anode side. This improvement not only significantly lowers the cost of the PIB but also effectively lessens the overall weight of the battery pack.[6] However, although some significant research work has been carried out,[4,7–12] the development and application of PIBs are still in the toddler stage. At present, considerable research work has been devoted to carbon materials because of their excellent electrical conductivity and high cost-benefit effectiveness.[13–20] However, the inherent defects of low theoretical specific capacity limit its further development.[21–23] Therefore, the development of ideal PIB anode materials with high specific energy and long-life is a pressing issue that needs to be overcome.

Transition metal sulfides have long been regarded as promising anode materials for secondary ion batteries owing to productive two-dimensional interlayer channels and numerous active sulfur sites;[8,24–28] however, only a few typical metal sulfides ($CoS$,[10] $SnS_2$,[11] $MoS_2$,[12,29] $VS_2$,[30] $SnS$,[31] *etc.*) have received researcher's attention and been investigated in PIBs. Among such transition metal sulfides, nickel disulfide ($NiS_2$) has rarely been empirically studied for its potassium-ion storage behaviour. Different from the intercalation reaction behaviour exhibited by graphite, $NiS_2$ is a typical pyrite-type structure compound,[32] which exhibits a conversion reaction mechanism during the potassiation/de-potassiation process, thereby

[a]*School of Materials Science and Engineering, State Key Laboratory of Advanced Technology for Materials Synthesis and Processing, Wuhan University of Technology, 122 Luoshi Road, Wuhan, 430070 Hubei, China. E-mail: mlq518@whut.edu.cn*
[b]*Department of Physical Science & Technology, School of Science, Wuhan University of Technology, 122 Luoshi Road, Wuhan, 430070 Hubei, China. E-mail: wxp122525691@whut.edu.cn*
†Electronic supplementary information (ESI) available. See DOI: 10.1039/d0nr01274b

showing three times high theoretical capacity (*ca.* 870 mA h $g^{-1}$) compared to graphite. Nevertheless, the unstable sulfur electrochemistry during cycling and the inherently slow kinetic properties of metal sulfide result in fast capacity decay and inferior rate performance.[32–35] One useful way to promote the improvement of electrochemical performance is to rationally design nanostructures with large surface areas and short ion diffusion pathways.[36–40] Another effective solution against these drawbacks is to combine the nanostructured $NiS_2$ with a conductive carbon matrix.[8,10–12,26] Recently, Ji and co-workers reported hierarchical flowerlike $NiS_2$ decorated with a multi-functional carbon anode material with enhanced cycling stability and rate performance,[41] further demonstrating the effectiveness of this strategy. However, due to the inherent complexity of the multi-electron transfer reaction process, the author's research on the structure and phase evolution of electrode materials still encounters some difficulties and lacks authentic evidence.

Herein, we designed a self-adaptive strain-relaxed PIB anode, which was constructed by three-dimensional graphene-supported nickel disulfide nanoparticles ($NiS_2$/3DGO). Such a hierarchical structure of $NiS_2$/3DGO greatly enhances ionic and electronic conductivity and makes full use of the transport capacity of an individual nanoparticle. Besides, the presence of 3DGO provides a highly elastic protective layer for the volume expansion of $NiS_2$ and effectively increases the electrostatic attraction to $S_2^{2-}$. When it is applied in PIBs, the as-obtained $NiS_2$/3DGO electrode exhibits an enhanced reversible capacity of 391 mA h $g^{-1}$ and remarkable rate behavior (260 mA h $g^{-1}$ at 1000 mA $g^{-1}$). Furthermore, with advanced *in situ* X-ray diffractometer and *ex situ* Raman technology, the structure evolution and phase transition mechanism of the nickel disulfide anode during potassiation/de-potassiation were systematically investigated. We believe that such understandings are indispensable for exploring the transition metal sulfide materials and give directions to design novel electrode materials for large-scale energy storage.

## Experimental

### The synthesis of a Ni(OH)$_2$ precursor

First, 3 mmol of $Ni(NO_3)_2 \cdot 6H_2O$ was first dissolved in 80 mL deionized water. Then, 2 mmol $NH_4F$ and 5 mmol urea were added to obtain a transparent green solution after stirring for 10 min. Then, the obtained solution was transferred into a Teflon-lined (100 mL) stainless-steel autoclave. The autoclave was heated at 120 °C and kept for 6 hours, and then naturally cooled. The obtained green precipitate was washed several times and then put into a 60 °C vacuum oven and dried for later use.

### The synthesis of NiS$_2$/3DGO

A self-adaptive strain-relaxed $NiS_2$/3DGO hybrid material was synthesized *via* facile *in situ* sulfurization and self-assembly processes. The prepared nickel-based precursor (80 mg) was redistributed in deionized water (30 mL). Subsequently, graphene oxide (GO) dispersion (5 mL, 2 mg mL$^{-1}$) was dissolved in it. Finally, an appropriate amount of thioacetamide (TAA) was added. Then, the as-obtained solution was transferred into Teflon-lined (50 mL) and kept for 8 hours at 180 °C. The black solid was repeatedly washed several times before vacuum drying at 80 °C overnight.

### The synthesis of NiS$_2$ microflowers

The method for synthesizing $NiS_2$ microflowers is the same as that for preparing $NiS_2$/3DGO. The difference is that the GO solution component is not introduced into the $NiS_2$ microflower synthesis process.

### Materials characterization

The microscopic characteristics of samples were investigated using a Japanese JEOL7100FA scanning electron microscope (SEM, 15–20 kV) and transmission electron microscopy with a scanning voltage of 200 kV (TEM, JEM-2100F). This equipment is also equipped with an X-ray energy spectrum analysis system, which can assist in the qualitative analysis of the chemical composition and distribution of materials. The D8 Advance powder X-ray diffractometer detected the structures of the as-prepared materials with Cu Kα. The corresponding voltage and current parameters are 20 kV and 10 A, respectively, and the test angle is 10–80°. Thermogravimetric analysis measurement (Netzsch STA 449C) was performed from 30 °C to 800 °C at a heating rate of 10 °C min$^{-1}$ to detect the content of $NiS_2$. Raman spectra were recorded using a Horiba Jobin Yvon Lab RAM HR800 Raman spectrometer with He–Ne laser excitation at 633 nm. X-ray photoelectron spectroscopy (XPS) was investigated using a VG Multilab 2000 system.

*In situ* X-ray diffractometer (XRD) was employed to analyze the crystal structure evolution and phase transition mechanism during the charging/discharging process. The XRD signals were acquired every 120 s using a Bruker D8 Discover X-ray diffractometer with a planar detector in still mode.

### Electrochemical measurements

Electrochemical characterization was performed using 2016 coin cells. The working electrode was prepared by applying a slurry containing $NiS_2$/3DGO or $NiS_2$ microflowers (70 wt%), acetylene black (20 wt%), and a sodium carboxymethyl cellulose (10 wt%) binder on an aluminium foil, respectively. Then, the coated aluminium foil was put in a vacuum oven and dried at 80 °C for 24 hours. The dried aluminium foil was further cut into small square slices with a diameter of 10 mm and a thickness of 100 μm, in which the average loading mass of $NiS_2$/3DGO or $NiS_2$ microflowers is about 1.0 mg cm$^{-1}$. The electrolyte used in the experiment was 1 M bis(fluorosulfonyl) imide potassium salt in ethylene carbonate/diethyl carbonate (EC : DEC = 1 : 1 Vol.%). The galvanostatic discharge/charge data measurement is performed using a LAND system. A Biologic VMP-3 electrochemical workstation was used to complete cyclic voltammetry and impedance testing.

# Results and discussion

The overall fabrication process of NiS$_2$ microflowers (NiS$_2$ MF) and NiS$_2$/3DGO is briefly illustrated in Fig. 1, including (i) the formation of 2D nickel hydroxide (Ni(OH)$_2$) microflower precursor (Fig. S1†) and (ii) the *in situ* sulfurization and self-assembly processes. During the sulfurization step, thioacetamide is uniformly dispersed in the solvent and reacts quickly with water to form H$_2$S at high temperatures. The produced H$_2$S reacts with the 2D nickel hydroxide nanosheets, resulting in the transformation from a 2D Ni(OH)$_2$ nanosheet template



**Fig. 1** Schematic illustration of the synthesis process for NiS$_2$/3DGO and NiS$_2$ MF and the proposed stabilizing effects of 3DGO on the NiS$_2$ electrode.

to NiS$_2$ nanoparticles (Fig. S2a†). Due to the lack of necessary bonding force between particles, the structure of NiS$_2$ MF is unstable and easy to collapse (Fig. S2b†). Interestingly, with the introduction of GO into the system, NiS$_2$ nanoparticles are preferentially nucleated and grown on the surface of GO[42] (Fig. S2c†). Meanwhile, the shrinking force generated by multi-layer self-assembly of GO firmly anchors nano-sized NiS$_2$ particles between GO layers[43] (Fig. S2d†). This unique structure not only provides a highly elastic protective layer to alleviate the massive volume expansion but also stabilizes the dissolution of sulfides in the electrolyte.[31]

XRD patterns were investigated to detect the phase and crystal structure information of the finally obtained samples (Fig. 2a). All characteristic diffraction peaks of both NiS$_2$ MF and NiS$_2$/3DGO can be well indexed with cubic pyrite NiS$_2$ (JCPDS No. 89-3058), manifesting the as-prepared Ni(OH)$_2$ precursor does successfully convert into NiS$_2$ after long-time sulfurization. No distinct diffraction peak located at 22.5° resulting from the (002) plane of the graphene nanosheets was detected in NiS$_2$/3DGO. This phenomenon was caused by the growth of nanocrystalline NiS$_2$ on the GO sheet surface, thus preventing the re-stacking of the GO sheet and covering the weak GO signal.[44] Meanwhile, based on Scherer's formula, the size of the NiS$_2$ nanoparticles can be further reckoned to be in the range of 100–120 nm, which in accordance with the particle size statistics shown in Fig. S3.† For NiS$_2$/3DGO, two weak



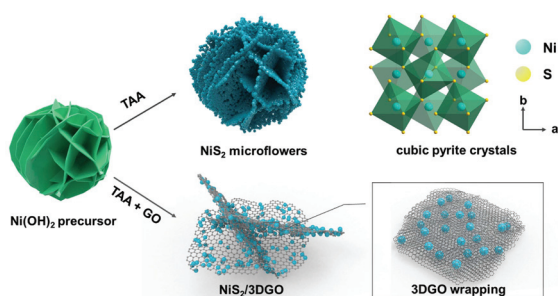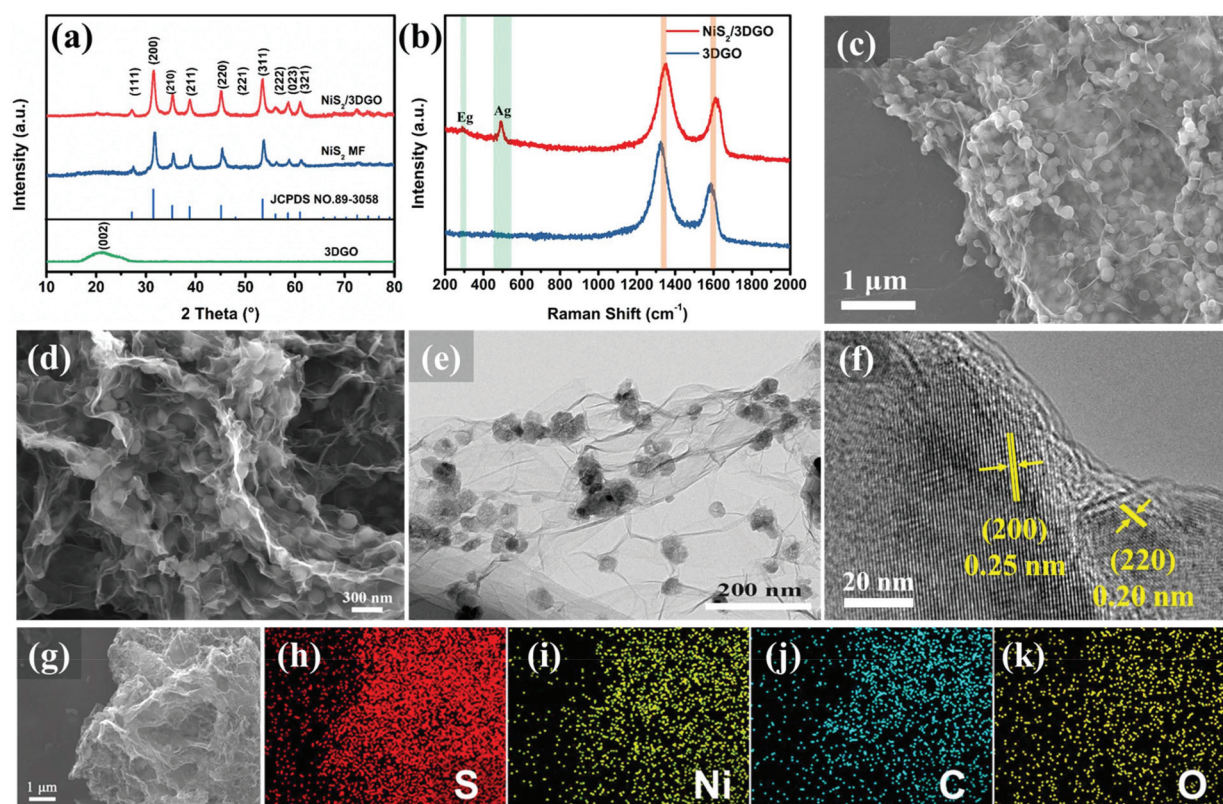**Fig. 2** (a) XRD comparison of NiS$_2$/3DGO, NiS$_2$ MF and 3DGO; (b) Raman spectrum of NiS$_2$/3DGO and 3DGO; (c and d) Representative SEM images of NiS$_2$/3DGO; (e and f) TEM and HRTEM images of NiS$_2$/3DGO; (g–k) SEM images and corresponding elemental mapping analysis of NiS$_2$/3DGO.

Raman peaks are detected at 289 and 490 cm$^{-1}$, which is attributed to $E_g$ and $A_g$ modes of NiS$_2$, respectively.[45,46] Besides, the Raman peaks at 1353 and 1608 cm$^{-1}$ are assigned to the D-band and G-band in GO.[47] The intensity ratio ($I_D/I_G$) of these two adjacent peaks is about 1.24 and lower than that of the 3DGO (1.44), confirming that more defects and disorder exists in the NiS$_2$/3DGO structure.[31] Meanwhile, the D and G peaks of 3DGO samples are shifted toward lower wavenumbers compared to those of NiS$_2$/3DGO samples, manifesting that the number of GO layers in 3DGO has increased significantly (Fig. 1b). This phenomenon further illustrates the fact that the presence of NiS$_2$ nanoparticles can effectively suppress the shrinkage of the GO layer.

The microscopic morphology of the NiS$_2$/3DGO is shown in Fig. 2c–f. Reprehensive SEM and TEM images show that NiS$_2$/3DGO composite exhibits a 3D interconnected structure and NiS$_2$ nanoparticles *in situ* nucleated and grown on the layers of the 3DGO substrate during the self-assembly process (Fig. 2c–e). Moreover, high-resolution TEM shows that the lattice fringes of NiS$_2$/3DGO exhibit interplanar spacings of 0.25 nm and 0.20 nm, which corresponds to the (200) and (220) planes of NiS$_2$, respectively (Fig. 2f). The corresponding elemental mapping of NiS$_2$/3DGO verifies that the Ni, S, C, and O elements were uniformly distributed in the hierarchical 3D interconnected structure (Fig. 2g–k and Fig. S4†).

The content of 3DGO in the as-prepared NiS$_2$/3DGO electrode was investigated by thermogravimetric analysis (TGA, Fig. S5†). The weight loss (2.92 wt%) occurring below 150 °C results in the vaporization of adsorbed water.[48] This part should be deducted during the calculation to reflect the authenticity of the result accurately. In the following stage, the weight loss and weight gain can be ascribed to the decomposition of 3DGO and the oxidation of NiS$_2$, respectively. Accordingly, the mass ratio of 3DGO in the NiS$_2$/3DGO composite is calculated to be 9.86%.

The surface chemical bonding states of Ni, S, C, and O in NiS$_2$/3DGO were further examined by XPS (Fig. 3a). Four peaks recorded at 284.6, 285.5, 286.7, and 288.6 eV can be separated from the C 1s spectrum (Fig. 3b), which corresponds to C=C, C–C, C–O, and O–C=O groups, respectively.[49,50] This further proved the existence of GO in NiS$_2$/3DGO. In Fig. 3c, two pairs of peaks can be detected at 856 and 874 eV, which is in agreement with 2p3/2 and 2p1/2 of Ni in cubic pyrite NiS$_2$.[41] Moreover, the S 2p spectra could be fitted to two adjacent peaks at 162.5 and 163.7 eV that is ascribed to 2p3/2 and 2p1/2 peaks for S$_2^{2-}$, respectively (Fig. 3d).

The electrochemical tests of the NiS$_2$ MF and NiS$_2$/3DGO hybrid electrode for potassium ion storage were evaluated ranging from 0.01 to 2.0 V (*vs.* K$^+$/K). A noticeable reduction peak appeared at ~1.0 V and disappeared in the subsequent cycles during the initial negative scan process (Fig. 4a). This process was ascribed to an amorphous intermediate phase K$_x$NiS$_2$ formed due to the original cubic NiS$_2$ lattice break and reconstructed during K$^+$ intercalation.[51] The following two reduction peaks at 0.68 V and 0.55 V are ascribed to the irreversible solid-electrolyte interface film (SEI) and the further
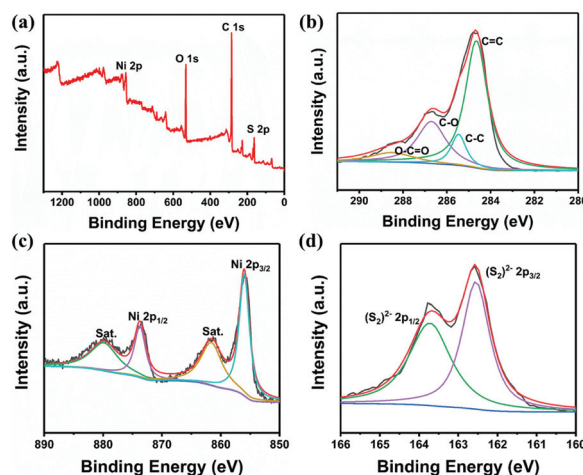


**Fig. 3** (a) The XPS survey spectra of NiS$_2$/3DGO; (b) C 1s; (c) Ni 2p; (d) S 2p.



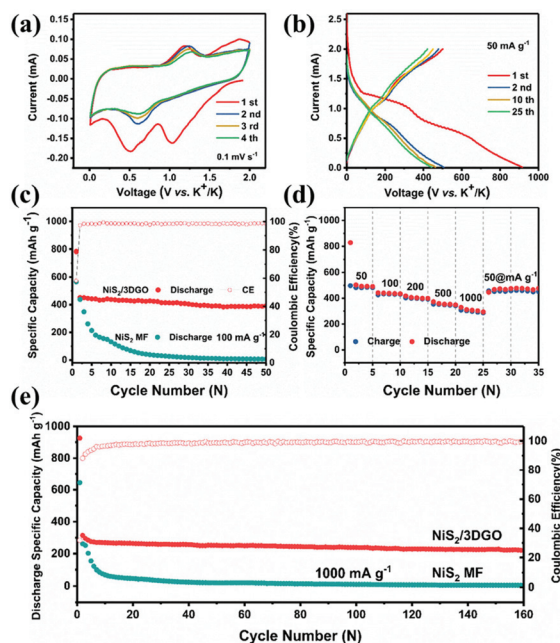**Fig. 4** (a) CV test result for the initial four cycles of NiS$_2$/3DGO at 0.1 mV s$^{-1}$. (b) Representative galvanostatic discharge/charge curves of NiS$_2$/3DGO at 50 mA g$^{-1}$. (c) Cycling performance of NiS$_2$/3DGO and NiS$_2$ MF at 100 mA g$^{-1}$. (d) Rate performance of NiS$_2$/3DGO at a different density. (e) Long-term cycling stability of NiS$_2$/3DGO at 1000 mA g$^{-1}$.

conversion process of K$^+$ with K$_x$NiS$_2$, respectively. For the reversed positive scan, two distinct peaks are detected at 1.18 V and 1.87 V, which are attributed to the conversion reaction of Ni$^0$ + K$_2$S$_4$ to form K$_x$NiS$_2$ and the further extraction of K$^+$ to form amorphous NiS$_2$, respectively. Both the oxidation peak and the reduction peak shifted slightly in the subsequent cycles, which indicates that an activation process may occur in

the initial cycle,[52] thereby achieving better K^{+} transport kinetics.

Fig. 4b and Fig. S6† show the comparison of galvanostatic discharge/charge (GDC) curves of the NiS₂/3DGO composite and NiS₂ MF anode at 50 mA g⁻¹, respectively. The NiS₂/3DGO sample showed a distinct higher discharge platform (1.0 V) and a highly consistent GDC curve compared to NiS₂ MF (0.8 V) during the charging/discharging process, manifesting that NiS₂/3DGO has much less polarization and better capacity retention compared to NiS₂ MF. According to the cycling performance of NiS₂/3DGO and NiS₂ MF at 100 mA g⁻¹ (Fig. 4c). The NiS₂/3DGO electrode showed a high initial discharge capacity with a reasonable initial coulombic efficiency (ICE) of 59%. The slightly low ICE is relative to the irreversible SEI and the reconstruction of original cubic NiS₂ lattice during K^{+} intercalation.[41] The NiS₂/3DGO electrode exhibits a high capacity retention of 88% after 50 cycles (compared with the second cycle). However, the cycling curve of NiS₂ MF without 3DGO supported shows an inferior cycling performance. Accurately, the NiS₂ MF only delivered a specific capacity of 793.5 mA h g⁻¹ with poor cycling performance. This result further demonstrates that the presence of the elastic GO protective layer dramatically enhances the structural stability of NiS₂/3DGO and makes full use of the transport capacity of individual NiS₂ nanoparticle.

When gradually increasing the current density at rate stages of 50, 100, 200, 500, and 1000 mA g⁻¹, the GDC curves remain stable and keep reversible capacities of 494, 398, 339, 283, and 235 mA h g⁻¹, respectively. When returning to 50 mA g⁻¹, the NiS₂/3DGO quickly recovers to a high specific capacity of 477 mA h g⁻¹ (about 97% capacity recovery rate). Moreover, NiS₂/3DGO still showed an excellent capacity retention of 260 mA h g⁻¹ after 160 cycles and high CE of approximately 100% at each cycle (Fig. 4e), far beyond the reversibility of NiS₂ MF (<20 mA h g⁻¹ after 50 cycles). Meanwhile, pioneering studies of typical transition metal sulphides were compared with our work. As shown in Table S1† and Fig. S7,† the obtained NiS₂/3DGO electrode had a competitive electrochemical performance in KIBs. Especially in the term of capacity, which is much better than those previously reported metal sulphide anodes. The EIS results verify that after the first discharge/charge, the impedance decreases significantly (Fig. S8†). After short activation, the impedance remained stable after 10, 30, and 50 cycles, which further proves that the NiS₂/3DGO electrode has a stable interface structure.

The kinetic research based on CV analysis at scan rates of 0.1 to 1.0 mV s⁻¹ is employed to acquire a deeper understanding of the outstanding rate performance of NiS₂/3DGO. Fig. 5a shows that the CV curve at each scanning speed shows similar peak positions and gradually broadened as the scan rate increases. These observations indicate that the NiS₂/3DGO electrode has typical pseudocapacitive potassium storage and excellent surface-dominated characteristics, allowing for ultrafast potassium ion insertion and extraction. A general method to measure the degree of pseudocapacitive effect is to make a
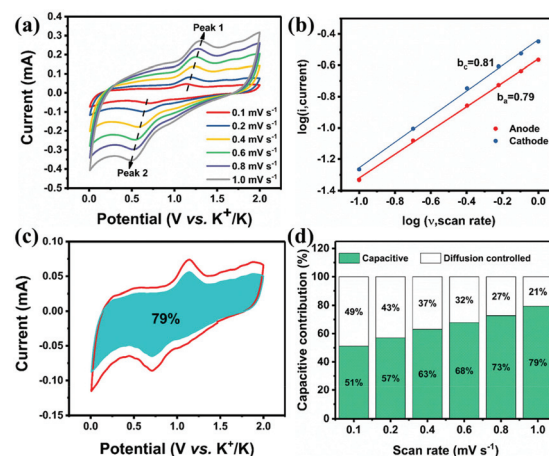


**Fig. 5** (a) CV curves of NiS₂/3DGO at scan rates range from 0.1 to 1.0 mV s⁻¹. (b) Linear relationship of log(i) vs. log(v). The contribution ratio of the capacitive capacities and diffusion-limited capacities at 1 mV s⁻¹ (c) and at different scan rates (d).

qualitative analysis based on the following equation: $i = av^b$, where $a$ and $b$ are constants.[53] Generally, for the ideal Faraday intercalation process controlled by the diffusion effect, the $b$ value is 0.5; for a surface-dominated process without diffusion control, the $b$ value is 1.0.[15] Hence, the higher $b$-value of NiS₂/3DGO (0.81/0.76) was determined by the cathodic/anodic peaks, suggesting a more favoured surface capacitance-dominated process of NiS₂/3DGO (Fig. 5b). Moreover, by further dividing the response current at the same potential into a surface-dominated process $(k_1 v)$ and a diffusion-dependent process $(k_2 v^{1/2})$ as the following equation: $i = k_1 v + k_2 v^{1/2}$, the percentage of capacitive contribution can be quantified. In consequence, 79% of the total capacity can be considered to be the capacitance contribution of the NiS₂/3DGO electrode at a scan rate of 1.0 mV s⁻¹, explaining the fundamental reason for the excellent rate performance of NiS₂/3DGO (Fig. 5c). Fig. 5d shows the investigation of the contribution of capacitance at all scan rates. As expected, the capacitance contribution is gradually increasing along with the scan rate. Such excellent pseudo-capacitive storage behaviour is primarily related to the abundant topological defects and excellent conductivity on the GO surface. It can maximize the surface charge storage and effectively improve the rapid pseudo-capacitive processes at the interface between NiS₂ and the electrolyte.[54]

In order to further reveal the phase transition process, in situ XRD analysis was performed. Fig. 6a shows that the as-fabricated NiS₂/3DGO electrode exhibits the characteristic peaks of (200), (210) and (211) at 31.5°, 35.3°, and 38.8°, respectively. When the cell discharged to 1.0 V, the intensity of each diffraction peak decreased clearly, suggesting that K^{+} is gradually inserted into the NiS₂ host material along with an intermediate phase KₓNiS₂ formation (Fig. 6a and Fig. S9†). The standard peak of NiS₂ disappears when discharged to 0.8 V. Simultaneously, an obvious peak well consistent with K₂S₄
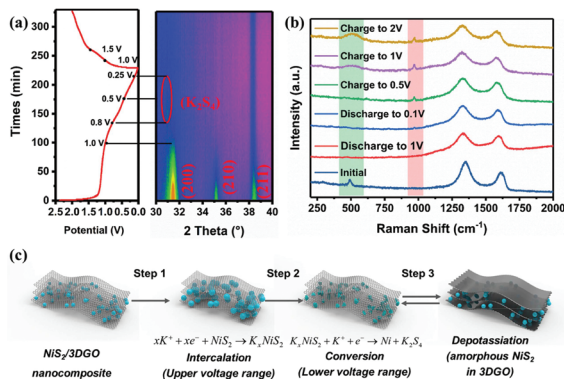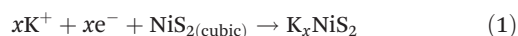
**Fig. 6** (a) *In situ* XRD results of NiS$_2$/3DGO during the first cycle at the cut-off voltage of 0.01–2.0 V. (b) *Ex situ* Raman spectrum of NiS$_2$/3DGO at different discharged/charged states. (c) Schematic illustration of the potassium storage mechanism.
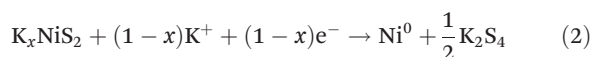
(JCPDS No. 43-0795) appeared at about 30.9°. The final product is K$_2$S$_4$ instead of K$_2$S, while Li$_2$S/Na$_2$S (analog of K$_2$S) is usually formed in LIBs/NIBs,[51,55] manifesting that the conversion reaction occurs and a new phase K$_2$S$_4$ and Ni$^0$ formation. No obvious metallic Ni characteristic diffraction peaks were observed in XRD. The reasonable interpretation is that the *in situ* formed Ni nanoparticles that are presumably smaller than the X-ray coherence length.[56] Moreover, no significant peak was observed during the subsequent charging process, suggesting an irreversible amorphous phase transition accompanied by the destruction of the original cubic NiS$_2$ lattice during K$^+$ intercalation. To confirm this point, *ex situ* Raman analysis was performed at different stages. As shown in Fig. 6b, with the progress of discharge, the intensity of NiS$_2$ characteristic peak reflection at 490 cm$^{-1}$ disappeared. Then, a broadening peak is observed when charged to 1 V, demonstrating that the original ordered cubic phase NiS$_2$ (denoted as NiS$_{2(cubic)}$) transformed into a disordered amorphous phase NiS$_2$ (denoted as NiS$_{2(amorphous)}$), which is consistent with the test results of *in situ* XRD. The Raman peak at around 245 cm$^{-1}$ was not detected, which may be ascribed to the addition of acetylene black and the binder reduced the Raman intensity of the original material. Interestingly, an additional Raman peak at 969.1 cm$^{-1}$ was detected when discharged to 0.1 V and kept persisting in the subsequent charging process, which may correspond to the SEI film formed during the initial cycle.[57] Therefore, the overall reaction process in the initial cycle was proposed as the following equation (Fig. 6c):

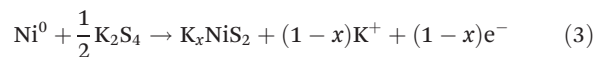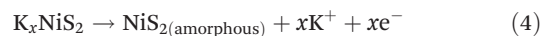During the discharging process:
From OCV to 1.0 V:

$$xK^+ + xe^- + NiS_{2(cubic)} \rightarrow K_xNiS_2 \qquad (1)$$

From 1.0 V to 0.2 V:

$$K_xNiS_2 + (1-x)K^+ + (1-x)e^- \rightarrow Ni^0 + \frac{1}{2}K_2S_4 \qquad (2)$$

During the charging process:
From 0.2 V to 1.2 V:

$$Ni^0 + \frac{1}{2}K_2S_4 \rightarrow K_xNiS_2 + (1-x)K^+ + (1-x)e^- \qquad (3)$$

From 1.2 V to 2.0 V:

$$K_xNiS_2 \rightarrow NiS_{2(amorphous)} + xK^+ + xe^- \qquad (4)$$

## Conclusions

In summary, a self-adaptive strain-relaxed NiS$_2$/3DGO hybrid electrode was fabricated through *in situ* sulfurization and self-assembly processes. NiS$_2$/3DGO presents a well-defined 3D conductive network in which 3DGO provides rich electronic conductive channels and effectively improves the rapid pseudocapacitive processes at the interface between NiS$_2$ nanoparticles and the electrolyte. Besides, the high flexibility and elasticity GO layer can be self-adaptive to the volumetric change of NiS$_2$. When applied in PIBs, NiS$_2$/3DGO exhibits high specific reversible capacity (451 mA h g$^{-1}$ at 50 mA g$^{-1}$), good cycling stability (260 mA h g$^{-1}$ at 1000 mA g$^{-1}$ after 160 cycles), and excellent rate performance (97% recovery ratio). Furthermore, the combination of *in situ* XRD and *ex situ* Raman observations confirmed that NiS$_2$ undergoes a deep conversion reaction of K$_x$NiS$_2$ to form K$_2$S$_4$ and Ni$^0$ during the initial cycle. This study describes the great potential of the NiS$_2$/3DGO electrode applied in PIBs and gives directions to design novel high-performance electrode materials.

## Conflicts of interest

There are no conflicts to declare.

## Acknowledgements

## Notes and references

1 S. Chu, Y. Cui and N. Liu, *Nat. Mater.*, 2017, **16**, 16–22.
2 Q. Liu, X. Su, D. Lei, Y. Qin, J. Wen, F. Guo, Y. A. Wu, Y. Rong, R. Kou, X. Xiao, F. Aguesse, J. Bareño, Y. Ren, W. Lu and Y. Li, *Nat. Energy*, 2018, **3**, 936–943.
3 M. Li, J. Lu, Z. Chen and K. Amine, *Adv. Mater.*, 2018, **30**, 1800561.
4 J. C. Pramudita, D. Sehrawat, D. Goonetilleke and N. Sharma, *Adv. Energy Mater.*, 2017, **7**, 1602911.
5 Y. Chen, L. Qin, Y. Lei, X. Li, J. Dong, D. Zhai, B. Li and F. Kang, *ACS Appl. Mater. Interfaces*, 2019, **11**, 45578–45585.

6   W. Zhang, Y. Liu and Z. Guo, *Sci. Adv.*, 2019, **5**, eaav7412.

7   Z. Jian, W. Luo and X. Ji, *J. Am. Chem. Soc.*, 2015, **137**, 11566–11569.

8   T. T. Shan, S. Xin, Y. You, H. P. Cong, S. H. Yu and A. Manthiram, *Angew. Chem., Int. Ed.*, 2016, **55**, 12783–12788.

9   K. Share, A. P. Cohn, R. Carter, B. Rogers and C. L. Pint, *ACS Nano*, 2016, **10**, 9738–9744.

10  H. Gao, T. Zhou, Y. Zheng, Q. Zhang, Y. Liu, J. Chen, H. Liu and Z. Guo, *Adv. Funct. Mater.*, 2017, **27**, 1702634.

11  V. Lakshmi, Y. Chen, A. A. Mikhaylov, A. G. Medvedev, I. Sultana, M. M. Rahman, O. Lev, P. V. Prikhodchenko and A. M. Glushenkov, *Chem. Commun.*, 2017, **53**, 8272–8275.

12  B. Jia, Q. Yu, Y. Zhao, M. Qin, W. Wang, Z. Liu, C.-Y. Lao, Y. Liu, H. Wu, Z. Zhang and X. Qu, *Adv. Funct. Mater.*, 2018, **28**, 1803409.

13  D. S. Bin, X. J. Lin, Y. G. Sun, Y. S. Xu, K. Zhang, A. M. Cao and L. J. Wan, *J. Am. Chem. Soc.*, 2018, **140**, 7127–7134.

14  W. Wang, J. Zhou, Z. Wang, L. Zhao, P. Li, Y. Yang, C. Yang, H. Huang and S. Guo, *Adv. Energy Mater.*, 2018, **8**, 1701648.

15  Y. Xu, C. Zhang, M. Zhou, Q. Fu, C. Zhao, M. Wu and Y. Lei, *Nat. Commun.*, 2018, **9**, 1720.

16  Y. Chen, L. Qin, Y. Lei, X. Li, J. Dong, D. Zhai, B. Li and F. Kang, *ACS Appl. Mater. Interfaces*, 2019, **11**, 45578–45585.

17  A. J. Naylor, M. Carboni, M. Valvo and R. Younesi, *ACS Appl. Mater. Interfaces*, 2019, **11**, 45636–45645.

18  Y. Zhao, X. Ren, Z. Xing, D. Zhu, W. Tian, C. Guan, Y. Yang, W. Qin, J. Wang, L. Zhang, Y. Huang, W. Wen, X. Li and R. Tai, *Small*, 2019, **16**, 1905789.

19  Y. Lei, D. Han, J. Dong, L. Qin, X. Li, D. Zhai, B. Li, Y. Wu and F. Kang, *Energy Storage Mater.*, 2020, **24**, 319–328.

20  Q. Yao, J. Zhang, J. Li, W. Huang, K. Hou, Y. Zhao and L. Guan, *J. Mater. Chem. A*, 2019, **7**, 18932–18939.

21  J. Li, N. Zhuang, J. Xie, X. Li, W. Zhuo, H. Wang, J. B. Na, X. Li, Y. Yamauchi and W. Mai, *Adv. Energy Mater.*, 2020, **10**, 1903455.

22  J. Xie, X. Li, H. Lai, Z. Zhao, J. Li, W. Zhang, W. Xie, Y. Liu and W. Mai, *Angew. Chem., Int. Ed.*, 2019, **58**, 14740.

23  Q. Yao, J. Zhang, J. Li, W. Huang, K. Hou, Y. Zhao and L. Guan, *J. Mater. Chem. A*, 2019, **7**, 18932–18939.

24  X. Ou, J. Li, F. Zheng, P. Wu, Q. Pan, X. Xiong, C. Yang and M. Liu, *J. Power Sources*, 2017, **343**, 483–491.

25  X. Ou, X. Liang, F. Zheng, P. Wu, Q. Pan, X. Xiong, C. Yang and M. Liu, *Electrochim. Acta*, 2017, **258**, 1387–1396.

26  P. Ge, H. Hou, S. Li, L. Yang and X. Ji, *Adv. Funct. Mater.*, 2018, **28**, 1801765.

27  Z. Li, J. Zhang, Y. Lu and X. W. D. Lou, *Sci. Adv.*, 2018, **4**, eaat1687.

28  J. Lu, Z. Chen, F. Pan, Y. Cui and K. Amine, *Electrochem. Energy Rev.*, 2018, **1**, 35–53.

29  Y. Han, W. Li, K. Zhou, X. Wu, H. Wu, X. Wu, Q. Shi, G. Diao and M. Chen, *ChemNanoMat*, 2020, **6**, 132–138.

30  J. Zhou, L. Wang, M. Yang, J. Wu, F. Chen, W. Huang, N. Han, H. Ye, F. Zhao, Y. Li and Y. Li, *Adv. Mater.*, 2017, **29**, 1702061.

31  X. Xiong, C. Yang, G. Wang, Y. Lin, X. Ou, J.-H. Wang, B. Zhao, M. Liu, Z. Lin and K. Huang, *Energy Environ. Sci.*, 2017, **10**, 1757–1763.

32  K. Liang, K. Marcus, S. Zhang, L. Zhou, Y. Li, S. T. De Oliveira, N. Orlovskaya, Y.-H. Sohn and Y. Yang, *Adv. Energy Mater.*, 2017, **7**, 1701309.

33  Q. Zou, Z. Liang, G. Y. Du, C. Y. Liu, E. Y. Li and Y. C. Lu, *J. Am. Chem. Soc.*, 2018, **140**, 10740–10748.

34  Q. Chen, S. Sun, T. Zhai, M. Yang, X. Zhao and H. Xia, *Adv. Energy Mater.*, 2018, **8**, 1800054.

35  Z. Zhao, Z. Hu, H. Liang, S. Li, H. Wang, F. Gao, X. Sang and H. Li, *ACS Appl. Mater. Interfaces*, 2019, **11**, 44333–44341.

36  B. Chen, Y. Meng, F. Xie, F. He, C. He, K. Davey, N. Zhao and S. Z. Qiao, *Adv. Mater.*, 2018, **30**, 1804116.

37  X. Wei, X. Wang, X. Tan, Q. An and L. Mai, *Adv. Funct. Mater.*, 2018, **28**, 1804458.

38  Y. Fang, X.-Y. Yu and X. W. D. Lou, *Matter*, 2019, **1**, 90–114.

39  A. Singh and V. Kalra, *J. Mater. Chem. A*, 2019, **7**, 11613–11650.

40  L. Wang, G. Yang, S. Peng, J. Wang, W. Yan and S. Ramakrishna, *Energy Storage Mater.*, 2019, **25**, 443–476.

41  L. Yang, W. Hong, Y. Zhang, Y. Tian, X. Gao, Y. Zhu, G. Zou, H. Hou and X. Ji, *Adv. Funct. Mater.*, 2019, **29**, 1903454.

42  W. Konicki, M. Aleksandrzak and E. Mijowska, *Pol. J. Chem. Technol.*, 2017, **19**, 120–129.

43  Y. Zhu, S. Murali, W. Cai, X. Li, J. W. Suk, J. R. Potts and R. S. Ruoff, *Adv. Mater.*, 2010, **22**, 3906–3924.

44  Q. Chen, W. Chen, J. Ye, Z. Wang and J. Y. Lee, *J. Power Sources*, 2015, **294**, 51–58.

45  T. Suzuki, K. Uchinokura, T. Sekine and E. Matsuura, *Solid State Commun.*, 1977, **23**, 847–852.

46  C. Zhang, *Int. J. Electrochem. Sci.*, 2017, **12**, 4610–4618.

47  R. Verma, P. N. Didwal, H.-S. Ki, G. Cao and C.-J. Park, *ACS Appl. Mater. Interfaces*, 2019, **11**, 26976–26984.

48  C. Zhang, Y. Xu, M. Zhou, L. Liang, H. Dong, M. Wu, Y. Yang and Y. Lei, *Adv. Funct. Mater.*, 2017, **27**, 1604307.

49  B. Li, Y. Liu, Y. Li, S. Jiao, S. Zeng, L. Shi and G. Zhang, *ACS Appl. Mater. Interfaces*, 2020, **12**, 2390–2399.

50  J. Zhang, Y. Xu, Z. Liu, W. Yang and J. Liu, *RSC Adv.*, 2015, **5**, 54275–54282.

51  G. Zhao, Y. Zhang, L. Yang, Y. Jiang, Y. Zhang, W. Hong, Y. Tian, H. Zhao, J. Hu, L. Zhou, H. Hou, X. Ji and L. Mai, *Adv. Funct. Mater.*, 2018, **28**, 1803690.

52  D. M. Zhang, J. H. Jia, C. C. Yang and Q. Jiang, *Energy Storage Mater.*, 2020, **24**, 439–449.

53  D. Chao, P. Liang, Z. Chen, L. Bai, H. Shen, X. Liu, X. Xia, Y. Zhao, S. V. Savilov, J. Lin and Z. X. Shen, *ACS Nano*, 2016, **10**, 10211–10219.

54  Y. Jiang and J. Liu, *Energy Environ. Mater.*, 2019, **2**, 30–37.

55  X.-C. Liu, Y. Yang, J. Wu, M. Liu, S. P. Zhou, B. D. A. Levin, X.-D. Zhou, H. Cong, D. A. Muller, P. M. Ajayan, H. D. Abruña and F.-S. Ke, *ACS Energy Lett.*, 2018, **3**, 1325–1330.

56  P. Poizot, S. Laruelle, S. Grugeon, L. Dupont and J. M. Tarascon, *Nature*, 2000, **407**, 496–499.

57  S.-L. Yang, H.-B. Yao, M.-R. Gao and S.-H. Yu, *CrystEngComm*, 2009, **11**, 1383–1390.